Boundary-Layer Meteorol
DOI 10.1007/s10546-012-9697-6

ARTICLE

Along-Coast Features of Bora Related Turbulence

Željko Večenaj · Danijel Belušić · Vanda Grubišić · Branko Grisogono

Received: 10 November 2010 / Accepted: 6 January 2012

Abstract The along-coast, offshore turbulence structure of the Bora flow that occurred on 7 November 1999 during the Mesoscale Alpine Programme (MAP) Intensive Observation Period 15 is examined. In this analysis we employ the aircraft and dropsonde data obtained over the Adriatic Sea, where the turbulence structure is determined by estimating turbulent kinetic energy (TKE) and its dissipation rate along the flight legs. The turbulence characteristics of Bora in the lee of the Dinaric Alps is greatly influenced by the mesoscale Bora flow structure over the Adriatic Sea, which in the cross-wind direction features an interchange of jets and wakes related to mountain gaps and peaks. In order to establish the origin of turbulence, the Weather Research and Forecasting—Advanced Research WRF (WRF-ARW) numerical model is used and its results are compared to the measurements. All five TKE-prediction parametrization schemes available in the model show reasonable agreement with the measured values. Since these parametrization schemes do not have horizontal advection included, they suggest that the along-flight structure of the Bora turbulence is principally generated by the local vertical wind shear. Further evidence is needed to support this hypothesis.

Electronic supplementary material The online version of this article (doi:10.1007/s10546-012-9697-6) contains supplementary material, which is available to authorized users.

Ž. Večenaj (✉) · B. Grisogono
Department of Geophysics, Faculty of Science, University of Zagreb, Zagreb, Croatia
e-mail: zvecenaj@gfz.hr
URL: www.gfz.hr

D. Belušić
School of Mathematical Sciences, Monash University, Melbourne, Victoria, Australia

V. Grubišić
Department of Meteorology and Geophysics, University of Vienna, Vienna, Austria

V. Grubišić
Earth Observing Laboratory, National Center for Atmospheric Research, Boulder, CO, USA

Journal: 10546-BOUN Article No.: 9697 MS Code: BOUN913.2 TYPESET DISK LE CP Disp.:2012/1/14 Pages: 19 Layout: Small

Keywords Adriatic Sea · Bora wind · Dissipation rate · Mesoscale Alpine Programme · Turbulence averaging interval · Turbulent kinetic energy · WRF-ARW model

1 Introduction

In the lee of the complex terrain of the Dinaric Alps, a well-known strong and gusty downslope flow called Bora extends from the north-eastern quadrant perpendicular to the mountain ridges (e.g. Jurčec 1981; Smith 1987; Klemp and Durran 1987; Poje 1992; Grubišić 2004). Bora may be induced by different synoptic conditions (e.g. Jurčec 1981; Poje 1995; Heimann 2001), and occurs most frequently during the winter season with a duration of several hours to several days (e.g. Enger and Grisogono 1998; Jeromel et al. 2009). It possesses a wide spectrum of average wind speeds; and due to its gustiness the wind-speed maxima may surpass 60 m s^{-1} (e.g. Belušić and Klaić 2006; Grisogono and Belušić 2009).

The Dinaric Alps extend along the eastern Adriatic coast from north-west towards south-east. The mountains separate the narrow coastal zone from the inland region (Fig. 1), and their width and maximum height increase from north-west to south-east. The peaks range from 1–1.7 km in height in the northern to 1.5–2 km in the southern part. Along the northern part of the eastern Adriatic coast the mountain ranges rise rapidly above the Adriatic Sea, providing a mountain profile with a long, moderate upwind slope and a short steep leeside slope. Also, this is where the Dinaric Alps are the narrowest with several pronounced peaks and gaps. Since Bora flows in the direction perpendicular to this mountain range, the airflow experiences a strong influence of the terrain complexity.

A detailed review of recent advances in understanding the severe Bora wind can be found in Grisogono and Belušić (2009). They emphasize that the progress in Bora research over the first decade of the twenty-first century has mostly been concentrated on scales ranging from mesoscale to microscale. These include the three-dimensional structure of the Bora flow (Grubišić 2004) and phenomena such as lee-wave rotors (e.g. Gohm et al. 2008) and gust pulsations (Belušić et al. 2004, 2007). Many studies based on mesoscale numerical models, both hydrostatic and non-hydrostatic, have been published on the Bora subject, and

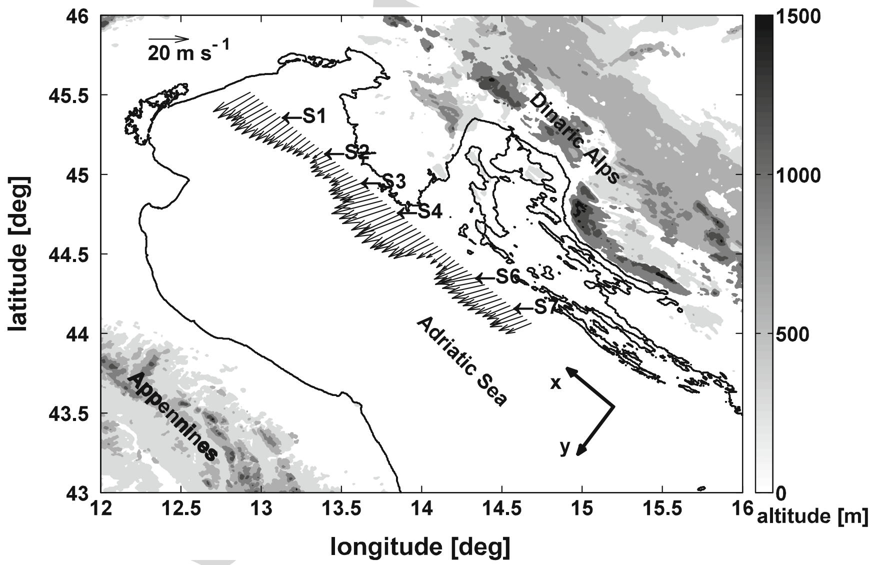

Fig. 1 Area of interest, the lower flight leg (370 m a.s.l., flown from 1504 to 1539 UTC 7 November 1999) with wind vectors (1.6-km averages) and the release positions of dropsondes. Reference wind vector is shown in the *top left corner*, while the orientation of the coordinate system is denoted in the *bottom right corner*

most of them simulate the basic Bora structure quite well (Klemp and Durran 1987; Enger and Grisogono 1998; Klaić et al. 2003; Grubišić 2004; Jiang and Doyle 2005; Belušić et al. 2007; Gohm et al. 2008; Telišman Prtenjak and Belušić 2009; Horvath et al. 2009; Trošić and Trošić 2010). As for the small-scale features, i.e. turbulence, as stated in Gohm et al. (2008) and Grisogono and Belušić (2009), numerical simulations may be doubtful because of the sensitivity of the model results to different turbulence parametrization schemes. An example of a model's inability to correctly reproduce the amount of observed turbulence is given in Belušić and Klaić (2006).

In order to evaluate simulated small-scale features, a proper set of observations that would allow a comparison of simulations with real flows is needed. Some in-situ, single-point near-surface high-frequency data suitable for such a purpose exist, measured in the town of Senj on the eastern Adriatic coast (Belušić et al. 2006; Večenaj et al. 2010). The first of these studies used 1-Hz data provided by a cup anemometer to explore the relationship between the high-frequency wind variance and the mean Bora flow. In the second study, 4-Hz ultrasonic anemometer data were used to estimate turbulent kinetic energy (TKE) and its dissipation rate (ε) near the surface. Besides these two datasets from ground-based instruments, there are airborne high-frequency datasets available from the Alpine Experiment (ALPEX) in 1982 and the Mesoscale Alpine Programme (MAP) in 1999 that are also suitable for the investigation of small-scale features of the Bora. Mahrt and Gamage (1987) used the ALPEX data to investigate turbulence characteristics parallel to the mean Bora flow in the nocturnal boundary layer, and were able to distinguish several types of turbulence in those conditions. While Grubišić (2004) used aircraft data from MAP to describe the mesoscale features of the Bora flow related to the underlying orography (with the emphasis on potential vorticity), we use the same data source here to describe small-scale turbulence features along the eastern Adriatic coast during the related severe Bora event.

In the first part of this paper the datasets used for the analysis are introduced and the scale of turbulence is investigated (Sects. 2, 3). In the second part, the results of the turbulence analysis are discussed and compared with the WRF ARW model output (Sects. 4, 5). Section 6 presents our concluding remarks.

2 Observational Data

The observational data analyzed here were collected during the MAP Intensive Observation Period 15 (IOP 15) on 7 November 1999 (e.g. Bougeault et al. 2001). During IOP 15, a strong Bora developed in the lee of the Dinaric Alps. The data were collected by the National Center for Atmospheric Research (NCAR) Electra aircraft flying a research mission offshore over the northern Adriatic Sea (Grubišić 2004). As part of this mission, two 216-km long flight legs were flown; the higher at approximately 680 m a.s.l. flying from south-east to north-west between 1429 and 1501 UTC, and the lower at approximately 370 m a.s.l. from north-west to south-east between 1504 and 1539 UTC. The data were sampled at a frequency of 25 Hz. The aircraft flew at a mean speed of 100 m s^{-1}, which corresponds to a raw spatial data resolution of approximately 4 m along the straight flight legs. Also, prior to the above two flight segments, nine dropsondes were released by the Electra aircraft along a flight leg at ≈4200 m a.s.l. flying from north-west to south-east between 1347 and 1420 UTC. Only the data from six dropsondes, which operated reliably all the way to the surface, are used here. Further, in the text and figures, these dropsondes are marked as S_j, where $j = 1, 2, 3, 4, 6$ and 7. The area of interest, the lower flight leg with the wind vectors, and the release positions of the dropsondes are shown in Fig. 1.

Journal: 10546-BOUN Article No.: 9697 MS Code: BOUN913.2 ☐ TYPESET ☐ DISK ☐ LE ☐ CP Disp.:2012/1/14 Pages: 19 Layout: Small

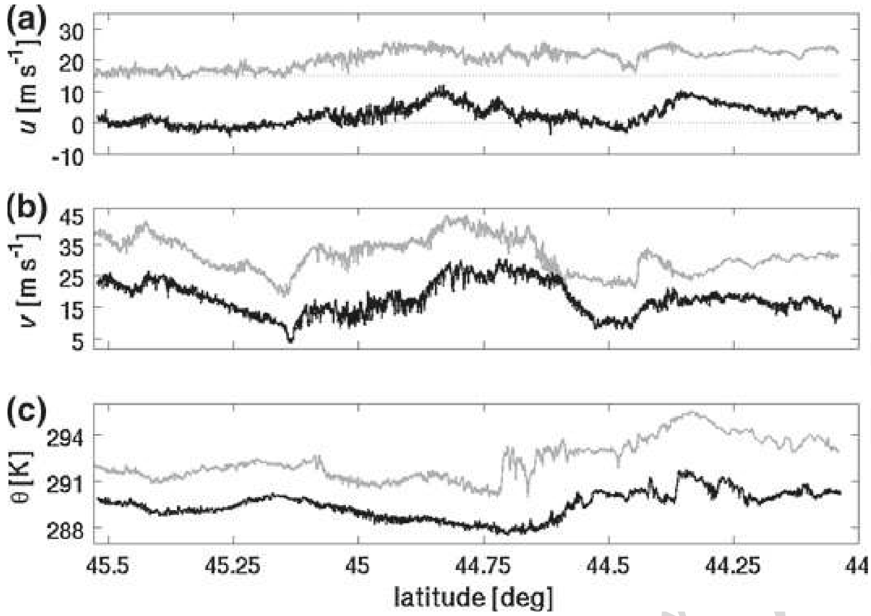

Fig. 2 Spatial features along the lower (370 m a.s.l., *black curve*) and higher (680 m a.s.l., *grey curve*) flight leg: **a** u component, **b** v component and **c** potential temperature θ. Values of (u, v) and θ at the higher flight leg are increased by 15 m s^{-1} and 2 K, respectively, for presentation. *Horizontal dotted lines* in panel **a** denote zero wind speed

We have chosen the right orthogonal coordinate system with the positive x-axis aligned parallel to the flight legs pointing towards the north-west (Fig. 1). This is in accordance with theory; particularly, turbulence theory regarding e.g. velocity correlations and spectra is mostly developed in the space domain where the longitudinal direction is the direction of the separation vector directed from one observation point toward the other (e.g. Batchelor 1959; Wyngaard 2010). Therefore, for aircraft measurements, the longitudinal direction should be parallel to the direction of the flight regardless of the direction of the mean flow (e.g. Lenschow et al. 1991).

The flight legs were designed to be perpendicular to the Bora flow. Based on the assumption that the typical Bora azimuth in this region is 040° (Grubišić 2004), the flight legs were flown at an azimuth of 130°. As seen in Fig. 1, the flight legs are almost perpendicular to the encountered Bora flow in the regions of the northern jet and the southern gap, while elsewhere the offset of ≈20° is present. The offset is due to the high degree of terrain complexity in the measurement domain.

Figure 2 shows the in situ flight-level data obtained by the Electra aircraft along the two legs flown at 370 and 680 m a.s.l. within the Bora layer. In accordance with the assumption that the flight legs are perpendicular to the wind, one would expect the values of the wind-speed component parallel to the flight legs, i.e. the longitudinal component (u), to be close to zero. The data displayed in Fig. 2a show a fair agreement with this assumption. The main feature of the wind-speed component perpendicular to the flight legs, i.e. the lateral or, in our case, transverse component (v), is the central, strong and wide north-easterly jet between 44.55°N and 44.90°N (Figs. 1, 2b) that is associated with the upwind terrain structure (Grubišić 2004). Likewise, there are two secondary jets, one at the northern end and the other at the southern end of the flight legs. The southern jet is accompanied by higher potential temperatures, θ (Fig. 2c).

The raw vertical profiles of the dropsonde data are shown in Fig. 3 (black lines). This shows that the central jet (displayed in Fig. 2a) is actually a part of the two- dimensional wind maximum structure that, going from north to south, abruptly ascends between S1 and S2

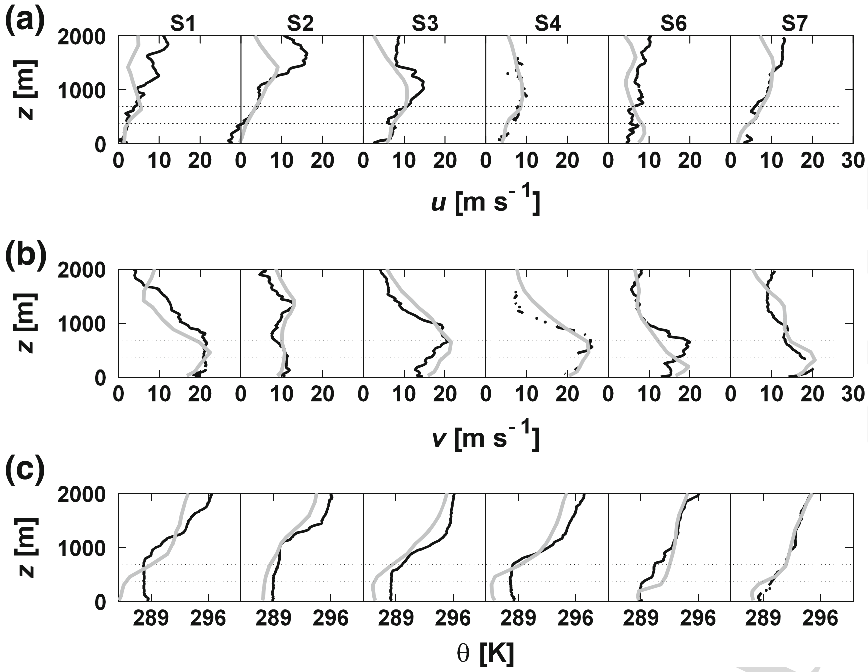

Fig. 3 Vertical profiles of the six dropsonde raw data (*black curves*) and the WRF-ARW BouLac simulation (*grey curves*; see Sect. 5) in the spatial order from *left to right* as they were released from north-west towards south-east (see Fig. 1): **a** u component, **b** v component and **c** potential temperature θ. *Horizontal dotted lines* mark the altitude of the flight legs

and gradually descends between S2 and S7 (Fig. 3a, b). Vertical profiles of θ (Fig. 3c) show that the layer between the flight legs at the northern section is unstable to near-neutral, while it becomes stable at the southern part. This is indicated in the aircraft data as well, by the difference in potential temperatures between the higher and lower flight legs that increases from north to south (Fig. 2c).

Throughout this study, we use two different datasets: the aircraft and the dropsonde data. These datasets were obtained up to two hours apart, so they can be compared to each other only if the Bora flow was stationary during that period. Based on numerical model results, it seems that the assumption of stationarity is reasonable for this case (see Sect. 5).

3 Determination of the Turbulence Averaging Interval

In order to define the flow turbulent perturbations that are needed for the calculation of TKE and turbulent fluxes, it is important to determine the scale that separates turbulence from the mean and/or mesoscale flow. This may be a non-trivial task, especially in the complex Bora flow where several scales interact (e.g. Grubišić 2004; Belušić et al. 2007; Gohm et al. 2008; Grisogono and Belušić 2009; Večenaj et al. 2010). Therefore, we first focus our efforts on finding a proper value of the averaging scale of the Bora turbulence.

3.1 Fourier Analysis

For nearly half of a century, the most common tool used for choosing the averaging interval in atmospheric flow has been the Fourier spectral analysis. According to e.g. Metzger and Holmes (2008), the averaging scale may be defined by an assumed spectral *energy gap* at the mesoscale. Therefore, we first apply the Fourier spectral analysis to the raw 25-Hz aircraft data. Power spectral densities of all three wind-speed components ($S_i(k)$) for both flight legs

Journal: 10546-BOUN Article No.: 9697 MS Code: BOUN913.2 TYPESET DISK LE CP Disp.:2012/1/14 Pages: 19 Layout: Small

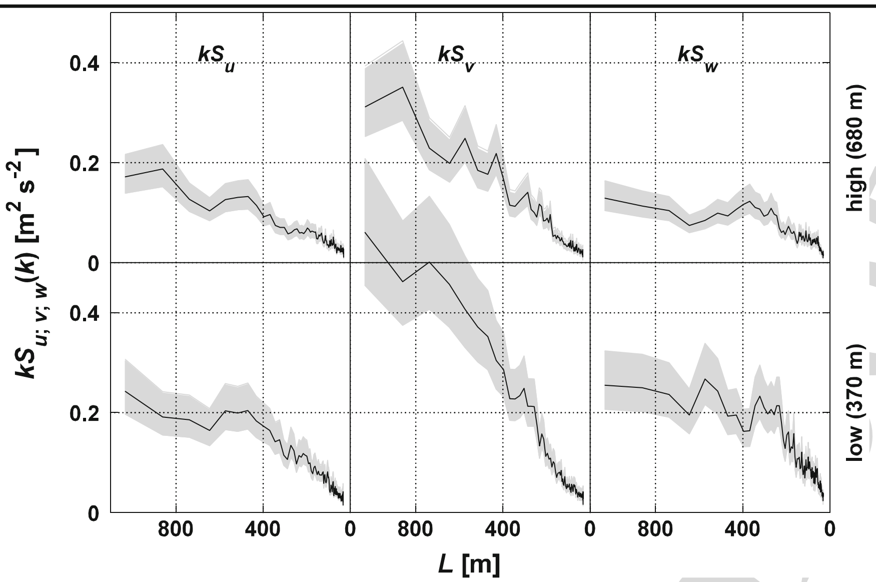

Fig. 4 A log-linear representation of weighted spectra (multiplied by the wavenumber k) for higher (*top curves*) and lower (bottom curves) flight legs (*black curves*) of all three wind-speed components. *Grey background area* denotes 95% confidence interval. Heights of flight legs are denoted on the right y-axis

in their entire length are calculated using the fast Fourier transform (FFT). These spectra are smoothed by block averaging spectral amplitudes using 52 windows with 50% overlap, where each window contains 1,024 data points that correspond to the length ≈4 km. On both flight legs, the spectra of the u component is characterized by a high level of noise at the high wavenumber end (starting from ≈0.25 m^{-1} up to the Nyquist value of 0.79 m^{-1}), which is manifested as a flat line in the log–log representation of the spectrum (not shown). According to Kaimal and Finnigan (1994), this kind of spectral behaviour is typical of the appearance of white noise in data, and which can be removed by simple block averaging. Therefore, the raw data were first block averaged to 5 Hz, which removed the unrealistic flattening of the spectrum, and then the 5-Hz data were used for all further analysis.

In order to find the *energy gap*, the spectra of all three wind-speed components, now using the 5-Hz data, were calculated using windows of 256 data points that correspond to the length ≈5 km (Fig. 4). The most promising candidate for the averaging scale is the gap around 600 m, seen in both u and w components at both higher and lower flight legs and in the v component at the higher flight leg. However, there are several more clearly emphasized gaps: at scales near 300 and 500 m in the spectrum of the v component at the higher flight leg, 300 and 900 m in the spectrum of the v component at the lower flight leg and 400 m in the spectrum of the w component at the lower flight leg. This makes it difficult to pinpoint a single averaging scale from the Fourier spectra, so we refer to other methods.

3.2 Multiresolution Flux Decomposition and the Ogives Method

The advantage of the multiresolution flux decomposition (MFD; Howell and Mahrt 1997) compared to the Fourier spectral analysis is that, while the peak in the Fourier spectra depends on the periodicity in data, the location of the peak in the MFD spectra is given by the length scale of the fluctuations; therefore, the periodicity in data is not required (Vickers and Mahrt 2003). The calculation of the MFD cospectra (D_{pq}, where p and q represent any two variables) involves windows with 2^m data points. Since we have averaged data to 5 Hz, the spatial resolution becomes 20 m and there are therefore 10,800 data points along 216-km long flight legs, which implies that the largest window for the MFD can contain $2^{13} = 8,192$ data

Journal: 10546-BOUN Article No.: 9697 MS Code: BOUN913.2 TYPESET DISK LE CP Disp.:2012/1/14 Pages: 19 Layout: Small

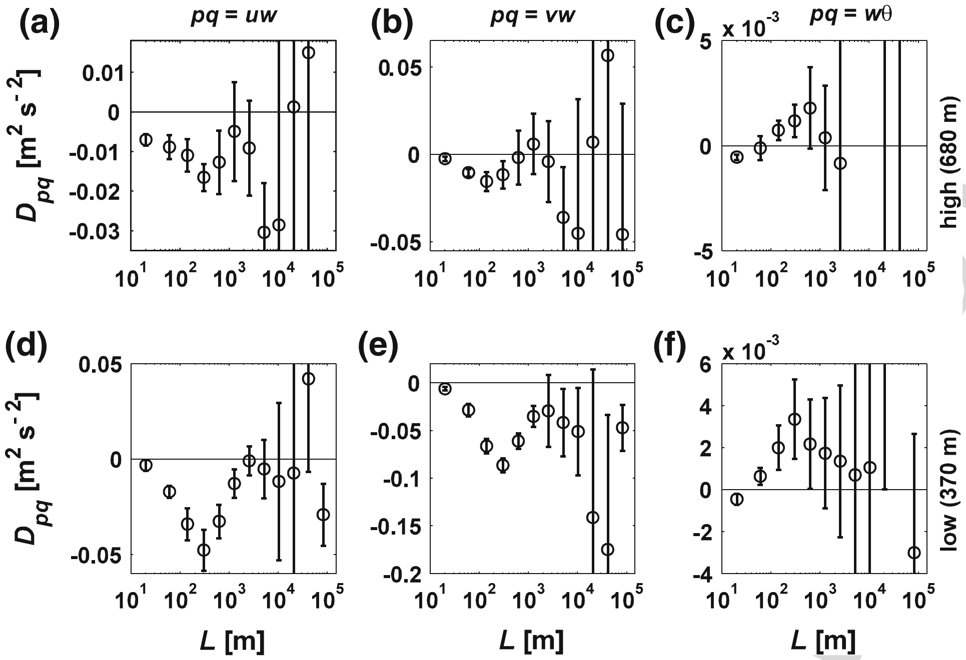

Fig. 5 Composite MFD cospectra (D_{pq}) of *uw*, *vw* and $w\theta$ fluxes at the higher **a–c** and lower **d–f** flight legs. *Vertical error bars* denote ± one standard deviation. Heights of flight legs are denoted on the right y-axis

points. Along the flight legs, 1000 D_{pq} for momentum (uw and vw) and heat ($w\theta$) fluxes are obtained by sliding the largest window every 40 m and the composite cospectra of these fluxes are constructed (Fig. 5). Following Vickers and Mahrt (2006), the averaging length scale can be determined as the last consecutive scale (coming from small toward larger scales), for which the composite D_{pq} does not yet change its sign (the sufficient condition is that the error bar crosses the zero-line). At the higher flight leg, D_{uw} and D_{vw} yield the scales of 620 and 300 m, respectively. At the lower flight leg, they both give the scale of 1,260 m. On the other hand, $D_{w\theta}$ shows strange behaviour at both flight legs, changing the sign already at the scale of 60 m and yielding the averaging scale of 20 m. Therefore, as with the Fourier analysis, the MFD cospectra do not provide conclusive results either.

Another way of searching for the averaging length scale using the MFD analysis is by using the cumulative MFD cospectra (ΣD_{pq}; Vickers and Mahrt 2003). If the cumulative MFD spectra show levelling off, i.e. if they start to locally converge after a certain length scale, this scale can be taken as the averaging scale. A similar criterion for the averaging scale is used with the Ogives technique (e.g. Oncley et al. 1996). Ogives (Og_{pq}) are based on the Fourier spectral analysis, and are defined as cumulative integrals of the Fourier cospectra of pq fluxes from the smallest towards the larger scales. If an ogive converges starting from a certain scale, this is an indication that there is no significant flux beyond this scale; thus, it may be taken as the averaging scale. The cumulative MFD cospectra and the ogives of both the momentum and heat fluxes for both flight legs are thus calculated (Fig. 6). The Fourier cospectra were determined using the procedure described in Sect. 3.1. At the higher flight leg, both ΣD_{uw} while ΣD_{vw} start to converge at the scale of 620 m (Fig. 6a), while at the lower flight leg this is the case only for ΣD_{vw}, while ΣD_{uw} diverges (Fig. 6c). The $\Sigma D_{w\theta}$ do not seem to converge on any flight leg (Figs. 6b, d); hence, it cannot be used for the determination of the averaging scale. A general feature of ogives is that they show similar behaviour as ΣD_{pq} but are shifted towards larger scales, and is also in accordance with Howell and Mahrt (1997). Therefore, while exhibiting somewhat less erratic behaviour than the previous techniques, this approach still fails to determine a single averaging scale.

Journal: 10546-BOUN Article No.: 9697 MS Code: BOUN913.2 TYPESET DISK LE CP Disp.:2012/1/14 Pages: 19 Layout: Small

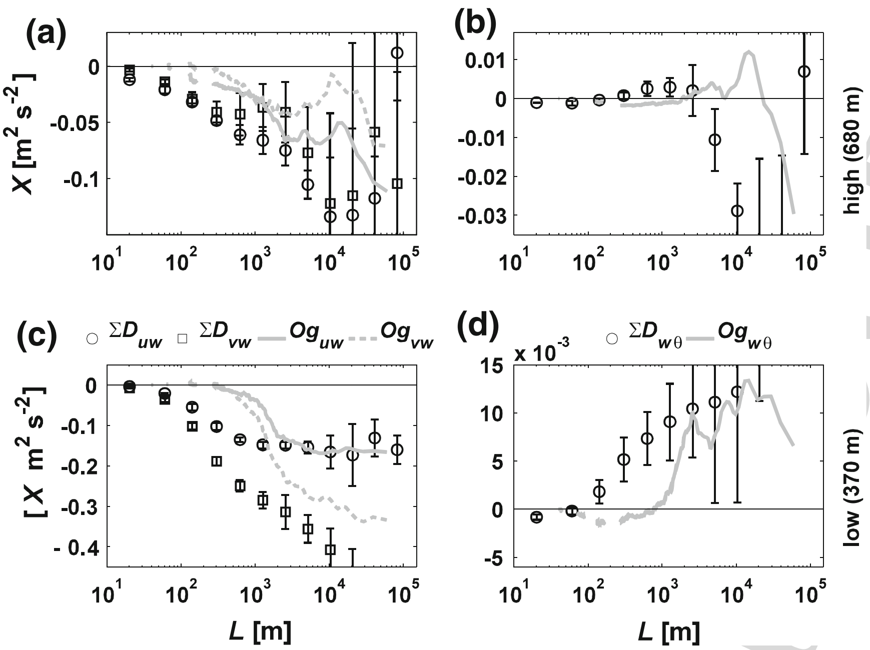

Fig. 6 Composite cumulative MFD cospectra (ΣD_{pq}) and ogives (Og_{pq}) of *uw* and *vw* fluxes on panels (**a**) and (**c**) and $w\theta$ fluxes on panels (**b**) and (**d**). *Vertical error bars* denote ± one standard deviation. Panels **a** and **b** are for the higher, while **c** and **d** are for the lower, flight legs. X on the y-axis stands for different variables. Heights of flight legs are denoted on the right y-axis

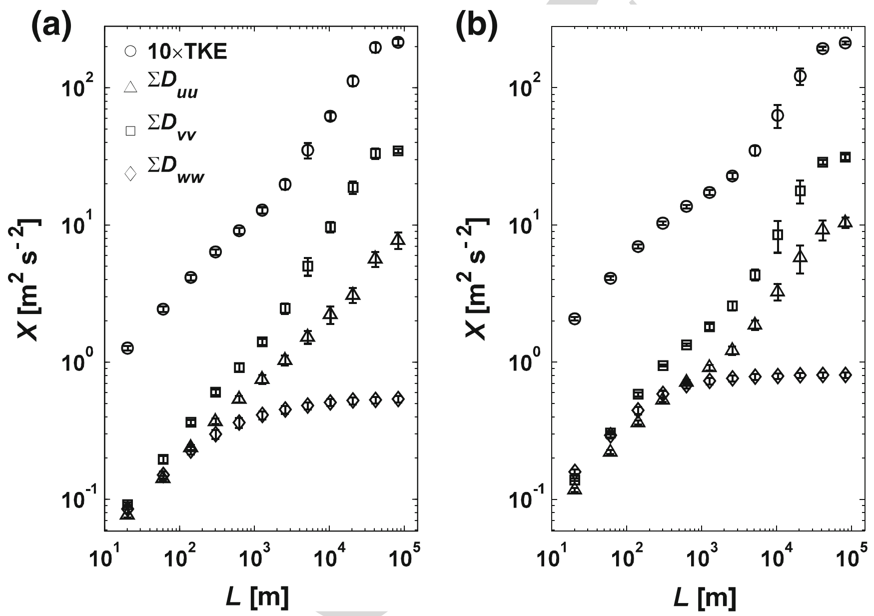

Fig. 7 Composite cumulative MFD variances (ΣD_{qq}) of all three wind-speed components and TKE for the higher (**a**) and lower (**b**) flight legs. Values of TKE are multiplied by a factor 10 for presentation. *Vertical error bars* denote ± one standard deviation. X on the y-axis stands for different variables

Finally, we turn to the examination of the TKE depending on the averaging length scale L. The cumulative MFD variances of all three wind-speed components (ΣD_{uu}, ΣD_{vv} and ΣD_{ww}) are used to calculate the TKE. Figure 7 shows that the TKE exponentially increases with the increasing averaging length scale. This is due to the growth of both u, and especially, v variances, which has a stronger effect on TKE than does the convergence of the w variance that starts at 1,260 m at the higher and 620 m at the lower flight leg. This is yet another indicator of how difficult it is to resolve the relevant scales in our data.

Journal: 10546-BOUN Article No.: 9697 MS Code: BOUN913.2 TYPESET DISK LE CP Disp.:2012/1/14 Pages: 19 Layout: Small

To summarize, there are indications that the energy gap could be located around 600 m. However, the results are not sufficiently unambiguous, and hence, they do not allow for the complete determination of the averaging scale. Therefore, we decide not to use the absolute values of TKE, but to concentrate only on the spatial variability of TKE along the flight legs.

4 Observed Turbulence Structure and Its Origin

4.1 Turbulent Kinetic Energy and Its Dissipation Rate

In the Cartesian system the mean TKE per unit mass, $\bar{e}$, is defined as a half of the sum of variances of all three wind-speed components:

$$\bar{e} = \frac{1}{2}\left(\overline{u'^2} + \overline{v'^2} + \overline{w'^2}\right), \tag{1}$$

where u', v' and w' are turbulent perturbations of the longitudinal, lateral and vertical wind-speed components, respectively, while the overbars represent suitable spatial averaging. Hereafter, in the text and corresponding figures, $\bar{e}$ will be referred to as TKE for simplicity. As explained in Sect. 3.2, we focus only on the spatial variability of TKE, and the flight legs are divided into 216 segments of 1-km length. For each segment, TKE is calculated using perturbations obtained by subtracting moving-average low-pass filtered data from the 5-Hz data on both flight legs. In order to test the dependence of the spatial variability of TKE on the averaging scale, three different lengths are used for the moving average (240, 500 and 1,000 m) and the obtained spatial distributions of TKE are normalized by the corresponding maximum values. As seen in Fig. 8a, the larger-scale spatial variability of TKE that is primarily related to major jets and wakes is maintained regardless of the averaging scale. However the smaller scale features may differ significantly, especially at the lower flight leg. Hence, the comparisons among turbulence quantities are more qualitative, and so we concentrate on the larger-scale spatial structure.

Two independent approaches are used for the evaluation of ε: the inertial dissipation technique and the third-order structure function (e.g. Piper and Lundquist 2004). A comparison of ε obtained by these two different methods provides an insight into the robustness of ε estimations. Both methods require the existence of the inertial subrange where turbulence is locally isotropic. According to e.g. Batchelor (1959) and Champagne (1978), a strong statement of the local isotropy is the 4/3 ratio of the lateral to longitudinal spectra $S_v(k)/S_u(k)$ and vertical to longitudinal spectra $S_w(k)/S_u(k)$. Figure 9a and b shows this ratio at the higher and the lower flight legs, respectively. While the $S_w(k)/S_u(k)$ ratio fluctuates around 4/3 starting from the length scale $L \approx 340$ m towards smaller scales on both flight legs, $S_v(k)/S_u(k)$ ratio exhibits a different behaviour. Namely, $S_v(k)/S_u(k) \geq 2$ at the scales larger than $\approx$ 200m and approaches one at smaller scales. The ratio $S_v(k)/S_u(k) \approx 2$ occurs because the lateral (streamwise) v, component carries most of the energy at larger scales (Figs. 7, 9c,d). The reason for the occurrence of the ratio of one at smaller scales is not clear at this point and should be further investigated. However, Biltoft (2001) shows that the convergence of both $S_v(k)/S_u(k)$ and $S_w(k)/S_u(k)$ to one is not rare in nature; moreover, he points out that, in general, there is no convincing experimental evidence that would support the existence of the theoretical 4/3 ratio. Therefore, we assume the presence of local isotropy and the inertial subrange in the corresponding range of data and continue with the estimation of ε. This assumption is to some extent supported by the presence of a $-5/3$ slope in the spectra of all three wind-speed components (Fig. 9c,d).

Journal: 10546-BOUN Article No.: 9697 MS Code: BOUN913.2 TYPESET DISK LE CP Disp.:2012/1/14 Pages: 19 Layout: Small

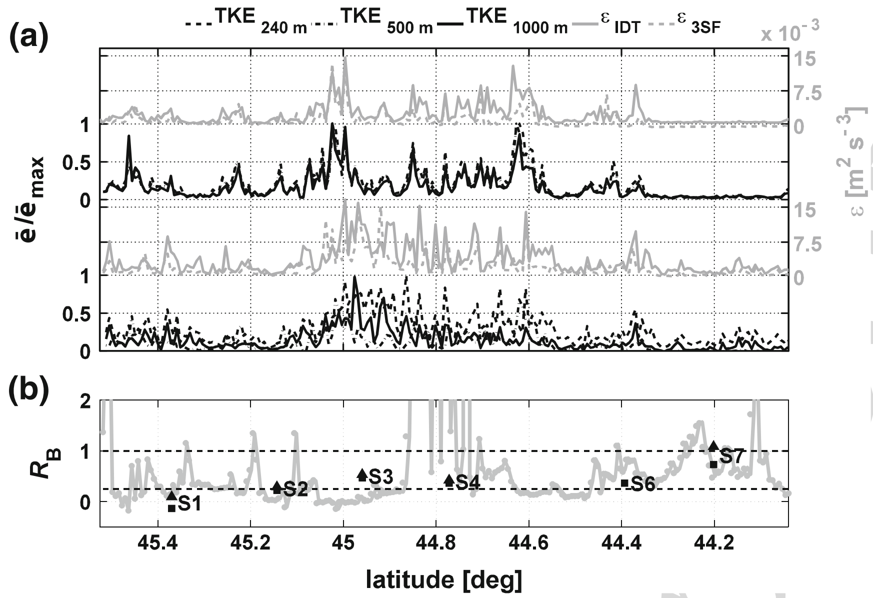

Fig. 8 (a) Spatial distributions of TKE normalized by its maximum value $\mathrm{TKE}_{\max}$ (*black curves*) and ε (*grey curves*) along the higher (*top curves*) and lower (*bottom curves*) flight legs. *Black dashed*, *dashed-dotted* and *solid curves* denote TKE calculated using 240, 500 and 1,000 m moving average, respectively. Values of $\mathrm{TKE}_{\max}$ are 0.98, 1.99 and 3.63 $\mathrm{m}^2\,\mathrm{s}^{-2}$ at the higher, and 1.28, 2.86 and 6.09 $\mathrm{m}^2\,\mathrm{s}^{-2}$ at the lower flight leg for 240, 500 and 1,000 m moving average, respectively. *Grey solid* and *dashed curves* denote ε estimated using the inertial dissipation technique and the third-order structure function, respectively. **b** Ri_B between the flight legs estimated using the aircraft data (*grey curve with dots*) and dropsonde data (*black triangles*). *Black squares* denote $\langle Ri \rangle$ between the flight legs estimated from the dropsonde data. *Horizontal dashed lines* denote Ri_c and Ri_T (see Sect. 4.2)

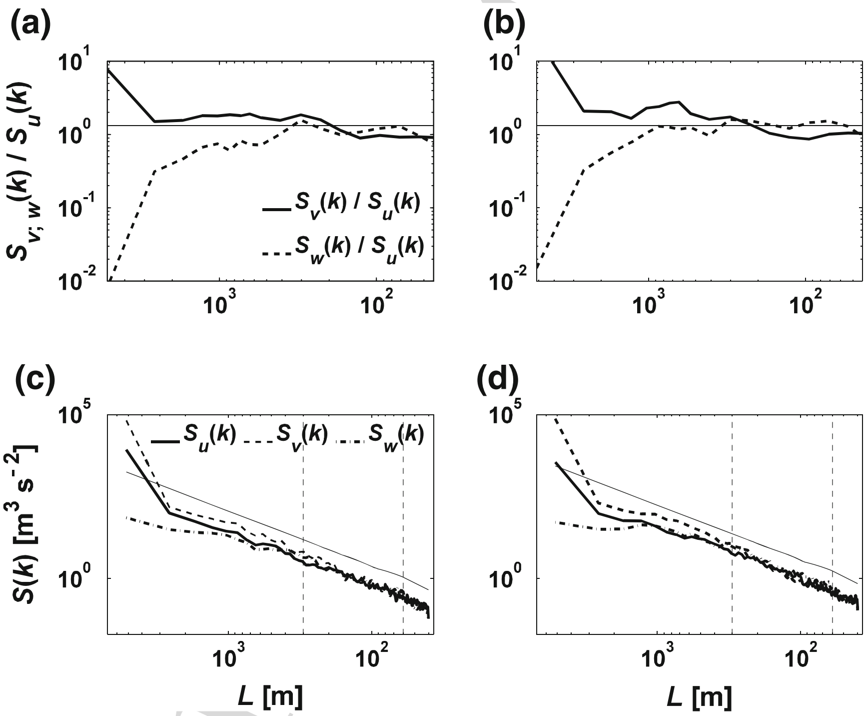

Fig. 9 The ratio between the streamwise v and longitudinal u spectra (*thick solid curve*) and between the vertical w and longitudinal u spectra (*thick dashed curve*) showing the approach to the 4/3 ratio required by local isotropy (*horizontal thin line*) for the higher (**a**) and the lower (**b**) flight legs. A log–log representation of u (*thick solid line*), v (*thick dashed line*) and w (*thick dashed-dotted line*) velocity spectra for the higher (**c**) and the lower (**d**) flight legs. The *thin solid line* is the $-5/3$ slope. *Vertical dashed lines* denote the length-scale interval of the closest spectra alignment with the $-5/3$ slope

The inertial dissipation technique is based on the Kolmogorov 1941 hypothesis (e.g. Tennekes and Lumely 1972), whereby the power spectra of the velocity components follow the $-5/3$ law in the inertial subrange (e.g. Stull 1988; Večenaj et al. 2011):

$$\log\left[S_i\left(k\right)\right] = -\frac{5}{3}\log k + \log\left(\alpha_i \varepsilon^{2/3}\right), \tag{2}$$

where $S_i(k)$ and α_i are the power spectrum and Kolmogorov constant for a particular velocity component, respectively, and k is the wavenumber. Several authors (e.g. Champagne 1978; Mestayer 1982; Večenaj et al. 2010, 2011) show that the $-5/3$ law for the velocity components spectra can be extended even outside of the inertial subrange toward larger scales. Re-arranging Eq. 2, ε can be evaluated as (e.g. Stull 1988):

$$\varepsilon = \left[\frac{k^{5/3} S_i\left(k\right)}{\alpha_i}\right]^{3/2}. \tag{3}$$

For each 1-km long segment, which contains 50 data points, FFT spectra of all three wind-speed components are calculated using windows of 32 data points. Then, ε is evaluated in the wavenumber band that corresponds to the length scales between 60 and 300 m, because there the spectra follow the $-5/3$ law (Fig. 9c,d). The value of the constant α_u is taken to be 0.53 (e.g. Champagne 1978; Oncley et al. 1996; Piper and Lundquist 2004) and, as expected in the inertial subrange, the other two constants are $\alpha_v = \alpha_w = (4/3)\alpha_u$. The values of ε so obtained by applying the inertial dissipation technique to different wind-speed components, and with this choice of Kolmogorov constants, compare well between themselves (not shown). In further analysis, only the values obtained from the u component will be used.

The third-order structure function (S_F) technique is based on the Kolmogorov 4/5 law defined on the longitudinal, u component (e.g. Albertson et al. 1997):

$$3S_F = \overline{\Delta u^3} = \overline{\left[u\left(x+r\right) - u\left(x\right)\right]^3} = \frac{4}{5}\varepsilon r, \tag{4}$$

which, when rearranged, gives the form of ε:

$$\varepsilon = \left(\frac{5}{4}\right)\frac{\overline{\Delta u^3}}{r}, \tag{5}$$

where r represents the spatial distance between the two measurements and the overbar denotes the averaging. According to Eq. 4, linear dependence of the structure function on r is expected in the inertial subrange. We found that for all segments on both flight legs this linear dependence is present at least for r between 20 and 480 m; thus, we use r from this interval for the evaluation of ε.

It is apparent from Fig. 8a that the values of TKE and ε are higher in areas where the lateral v component, indicates the presence of the north-easterly jet (Fig. 2a). Also, both TKE and ε are greater at the lower leg compared to that at the higher flight leg. The TKE and ε patterns follow each other closely, especially along the higher flight leg. This indicates a high degree of robustness in the estimate of ε, which is corroborated by a satisfactory agreement of ε values obtained from the two different techniques.

4.2 Origins of the Turbulence

Bora flow is associated with several specific characteristics that may influence the turbulence structure at the location of the aircraft measurements. First, the wave breaking induces a turbulent zone above the lee of the mountain range. While the aircraft flew offshore about

Journal: 10546-BOUN Article No.: 9697 MS Code: BOUN913.2 TYPESET DISK LE CP Disp.:2012/1/14 Pages: 19 Layout: Small

50 km distant from the mountain range and the wave-breaking turbulent region, the strong Bora flow might have advected this turbulence over a considerable distance. Second, Bora is characterized by strong horizontal shear at the interfaces between the mesoscale jets and wakes, and the associated potential vorticity banners. This shear could also influence turbulence generation at specific locations. Finally, the relatively cold and stable continental Bora flow air sweeps over the relatively warm sea surface, which influences its stability profile and turbulence generation out over the sea. All these features may exist in addition to the usual local turbulence generation mechanisms, primarily the very strong vertical wind shear in the jet regions. Next, we examine the origins of the observed turbulence spatial pattern.

An insight into the nature of turbulence can often be gained by evaluation of the gradient Richardson number (*Ri*), defined in terms of the buoyancy (Brunt-Väisälä) frequency (N) and the vertical wind shear (e.g. Tennekes and Lumely 1972; Stull 1988):

$$Ri = \frac{g}{\theta_V}\frac{\partial\theta_V}{\partial z} \Big/ \left[\left(\frac{\partial U}{\partial z}\right)^2 + \left(\frac{\partial V}{\partial z}\right)^2\right], \quad (6)$$

where θ_v is the virtual potential temperature, g is the acceleration due to gravity, while U and V are the mean longitudinal and lateral wind-speed components, respectively well known. Additionally, two key values of *Ri* derived from theoretical studies and laboratory experiments are the critical Richardson number, $Ri_c = 0.25$, and the termination Richardson number, $Ri_T = 1$ (e.g. Stull 1988). For $Ri < Ri_c$, modelled laminar flow usually becomes turbulent. On the other hand, modelled turbulent flow typically becomes laminar when $Ri > Ri_T$ (e.g.Mellor and Yamada 1974; Stull 1988). Hence, there appears to be a hysteresis effect in *Ri* (e.g. Stull 1988). Although this pragmatic, traditional modelling approach is sometimes criticized because of its oversimplification and neglect of stratified turbulence under $Ri \gg 0$ conditions (e.g. Baklanov and Grisogono 2007; Mauritsen et al. 2007; Zilitinkevich et al. 2008; Grisogono 2010), it still provides a useful reference.

In order to determine whether turbulence is produced by the local vertical shear or buoyancy, TKE and ε are compared to the bulk Richardson number (Ri_B) from the aircraft measurements and dropsondes shown in Fig. 8b. Here, the aircraft Ri_B is calculated from Eq. 6 using a 1-km horizontal averaging interval [a reasonable choice because it is not much larger than the favorable scale of ≈600 m and, at the same time, is in accordance with the resolution of the WRF-ARW innermost domain (see Sect. 5)]. The vertical gradients are approximated by the differences between the two flight legs (e.g.Stull 1988); hence, the value of Ri_B is significantly influenced by the vertical distance between the flight legs (e.g. Balsley et al. 2008). For dropsondes, data points closest to the flight legs are used in the calculation of the gradients. This Ri_B will also be complemented by calculating the approximate gradient Richardson number, *Ri*, obtained from the vertical profiles at much higher vertical resolution, either from dropsondes (see later) or from the numerical model (see later). While the value of Ri_B for S6 exceeds 10, the remainder of the dropsonde values are in rather good agreement with the aircraft Ri_B values. In some areas with large values of TKE and ε, Ri_B exhibits values $\gg$1, which might indicate that the turbulence is not produced locally (Fig. 8a,b). Another, more plausible option, is that the vertical spacing between the flight legs is too large, so that certain important flow features may not be taken into account in the calculation of Ri_B. This can be inspected using the dropsonde data, since they enable the calculation of *Ri* as well as Ri_B. Figure 8b shows Ri_B and $\langle Ri\rangle$, both calculated from the dropsondes, where $\langle Ri\rangle$ is the mean *Ri* in the layer between the two flight legs. While for some dropsondes Ri_B and $\langle Ri\rangle$ are similar in magnitude (S2–S4), for others in Fig. 8b the difference is significant (S1, S7 and especially S6 where $Ri_B > 10$). This indicates the validity of the second option, that is, that

Journal: 10546-BOUN Article No.: 9697 MS Code: BOUN913.2 TYPESET DISK LE CP Disp.:2012/1/14 Pages: 19 Layout: Small

due to large spacing between the flight legs, Ri_B, as calculated here, is not a good indicator of local stability. Unfortunately, our dataset does not provide any further insight related to this issue. Therefore, we have sought more detailed information from the WRF-ARW model simulations.

5 Comparison of Observations with Simulations

WRF-ARW is an atmospheric, non-hydrostatic, fully compressible, primitive equation numerical model that can be used for simulations of a wide range of scales of motion ranging from planetary scales to small-scale turbulence (Skamarock et al. 2008). Here, three two-way nested model grids are used, with horizontal grid spacing of 9, 3 and 1 km, and 66×66, 112×112, and 226×229 grid points, respectively (Fig. 10). There are 86 vertical levels with their spacing gradually increasing towards the model top at 50 hPa. Initial and boundary conditions are obtained from the European Centre for Medium-range Weather Forecasts (ECMWF) analyses. The simulation starts with the initiation of the outermost grid at 1800 UTC 6 November 1999, while the second and third grid onset is 6 h after their respective parent grid. The simulation ends at 1800 UTC 7 November 1999. Five different planetary boundary-layer (PBL) parametrization schemes that solve the prognostic TKE equation are available in the version 3.1.1 of WRF-ARW (Table 1). The model results presented here consist of five simulations that differ only in the choice of one of the five PBL schemes, and the corresponding surface-layer scheme as provided in the model. All the results shown are taken from the innermost grid. The five PBL parametrization schemes used here do not include the horizontal advection of TKE, and are purely one-dimensional (1D), i.e. they solve only for the vertical mixing. The full TKE budget equation in this case reduces to:

$$\frac{\partial \bar{e}}{\partial t} = -\frac{1}{\rho}\frac{\partial}{\partial z}\rho\overline{w'e} - \overline{u'w'}\frac{\partial U}{\partial z} - \overline{v'w'}\frac{\partial V}{\partial z} + \frac{g}{T}\overline{w'\theta'} - \varepsilon, \tag{7}$$

where ρ is the air density and T is the temperature (e.g. Mellor and Yamada 1974; Stull 1988). Therefore, the model success in reproducing the main features of the along-flight TKE structure may indicate that the measured Bora turbulence is not advected from other

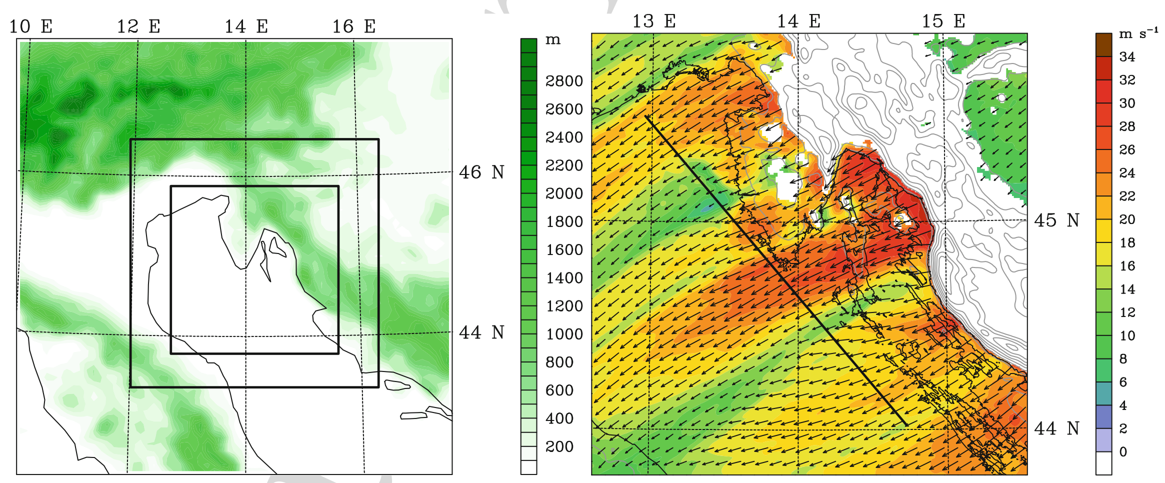

Fig. 10 WRF-ARW model grids used in this study. *Left panel* the outermost grid with 9-km grid spacing, with two nested grids indicated by *black squares*. The terrain is given every 100 m. *Right panel* the innermost grid with wind speed (*shaded*) and vectors at 374 m a.s.l. at 1500 UTC 7 November 1999, and the terrain with 200 m interval (*grey contours*). The *black line* denotes the aircraft flight legs

Table 1 PBL parametrizations used in WRF-ARW simulations

WRF simulation name	PBL parametrization
MYJ	Mellor-Yamada-Janjic (Janjić 1994)
QNSE	Quasi-normal scale elimination (Sukoriansky et al. 2005)
MYNN2.5	Mellor-Yamada Nakanishi and Niino Level 2.5 (Nakanishi and Niino 2006)
MYNN3	Mellor-Yamada Nakanishi and Niino Level 3 (Nakanishi and Niino 2006)
BouLac	Bougeault and Lacarrere (Bougeault and Lacarrere 1989)

regions nor is it generated by the horizontal shear. In that case, the individual terms in Eq. 7 provide the relative importance of shear and buoyancy in the TKE production. However, the PBL parametrizations may implicitly reproduce the effects of neglected processes, and therefore any related conclusions should be taken with care.

In the following, we compare the modelled and measured TKE. The model parametrization schemes used here are the ensemble-type of turbulence schemes, meaning that they theoretically incorporate the entire turbulence spectrum; in other words, all turbulence scales are considered unresolved. Therefore, they are not "subgrid", implying that the turbulence intensity does not depend on the model grid spacing. This is easily seen by intercomparing the three grids used here, where each parent grid has somewhat smaller TKE values than its child grid, primarily due to spatial smoothing of coarser grids (not shown). The latter obviously contradicts the "subgrid" argument, in which TKE values should decrease with decreasing grid spacing. Additionally, true subgrid schemes employ turbulence length scales that are proportional to the grid spacing. This is not the case with the ensemble schemes, such as those used here, because they use either Blackadar-type (distance from the surface) or flow-dependent length scale parametrizations (see e.g. Wyngaard 2004 for further discussion). For these reasons, we can safely conclude that the choice of the moving averaging length used to define turbulent perturbations from the data is not, and should not be, in any way dependent on the model grid spacing. However, since no unique averaging scale could have been determined for this dataset, we compare only the spatial structure of the normalized, dimensionless TKE, which makes it almost irrelevant as to which averaging scale is used (see Fig. 8). Here we choose 1 km for the averaging scale. On the other hand, the choice of the 1-km record length for the measurements (the flight legs are divided into 216 1-km records) is consistent with the model innermost grid spacing. The comparison is, hence, between the 1 km horizontal scale volume-averaged (model) and line-averaged (measurements) entire spectrum of turbulence, and in that respect it is consistent with comparisons of other scalars.

Since the aircraft flew the two selected flight legs between 1429 UTC and 1539 UTC, we have extracted the model output for three different times: 1430 UTC, 1500 UTC and 1530 UTC. Intercomparison of these three different output times indicates low sensitivity to the choice of the times (not shown), suggesting stationarity of the developed Bora flow structure during at least one hour. Therefore, we have chosen the 1500 UTC output time (which is approximately in the middle of the flight period) for comparison with the measurements. Fair agreement between the aircraft and dropsonde data along flight legs (Figs. 11, 12) supports the assumption of stationarity for the Bora flow. With respect to the mesoscale along-coast structure, the model reproduces the wind speed along the flight legs successfully for all simulations (Fig. 11a,b), though the agreement with the potential temperature is poorer (Fig. 12a,b). The model significantly underestimates θ on the northern half of the flight legs, which is probably due to the coarse resolution of the input sea-surface temperature that reduces the extent of

Journal: 10546-BOUN Article No.: 9697 MS Code: BOUN913.2 TYPESET DISK LE CP Disp.:2012/1/14 Pages: 19 Layout: Small

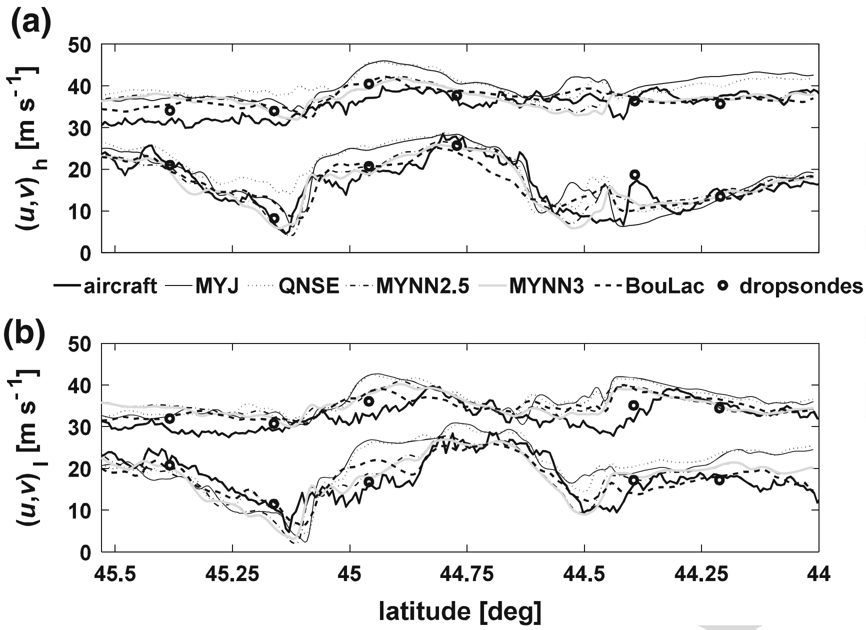

Fig. 11 Spatial distribution of modelled vs. measured u and v components at **a** higher (subscript h on the y-axis label) and **b** lower (subscript l on the y-axis label) flight legs. Longitudinal u component is above the transverse v component and is shifted by $30\,\mathrm{m\,s^{-1}}$ for presentation. The five model simulations are listed in Table 1. The modelled data are given for 1500 UTC 7 November 1999

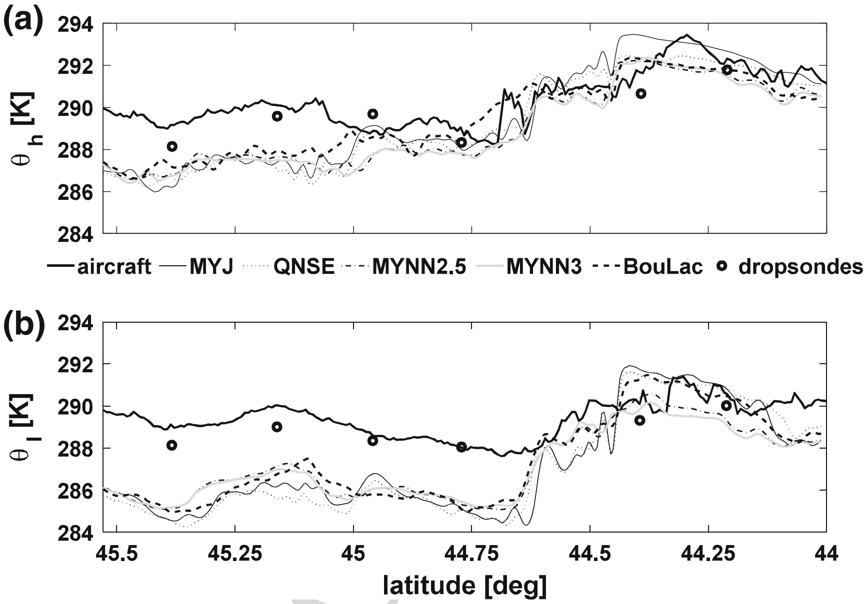

Fig. 12 Same as Fig. 11 but for potential temperature θ

the relatively warm Adriatic Sea in this border region. The normalized TKE structure varies considerably among different simulations (Fig. 13a,b), and it is hard to distinguish which simulation reproduces the most realistic spatial structure. The BouLac scheme (Table 1) is the only one that does not overestimate TKE in the southern parts of both flight legs, although it does underestimate TKE at the central part of the higher flight leg. As previously noted, the turbulence comparisons are performed mostly qualitatively and for larger-scale spatial structures, due to the uncertainty of the turbulence averaging length for the measurements (see Fig. 8a and the related discussion). We choose BouLac based simulation for the further analysis.

Journal: 10546-BOUN Article No.: 9697 MS Code: BOUN913.2 TYPESET DISK LE CP Disp.:2012/1/14 Pages: 19 Layout: Small

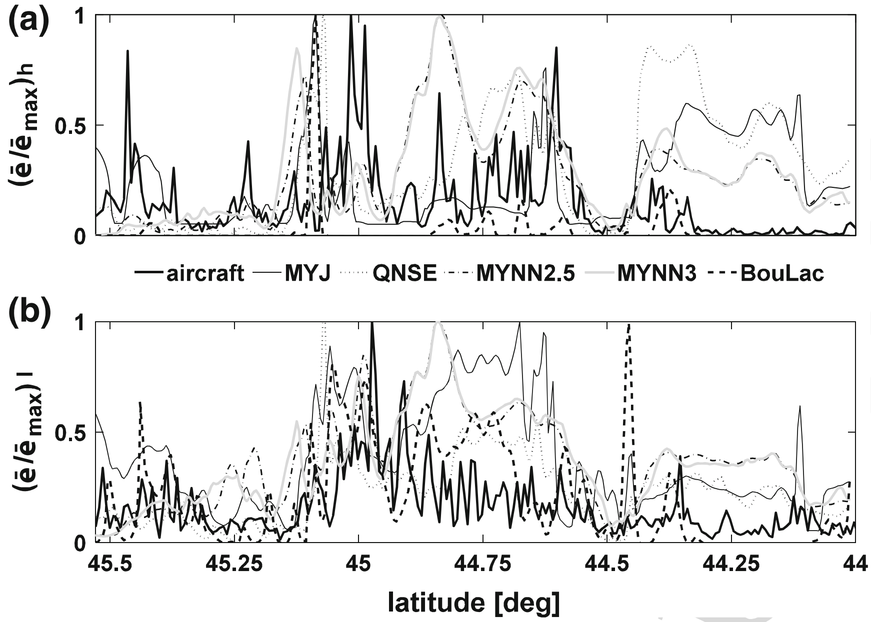

Fig. 13 Same as Fig. 11 but for the normalized TKE. For the aircraft data, TKE is calculated using the 1000-m moving average. Values of TKE_{max} are 3.63, 1.86, 1.36, 6.95, 6.34, and 2.63 $m^2\ s^{-2}$ at the higher, and 6.09, 1.99, 4.25, 5.29, 5.13 and 1.11 $m^2\ s^{-2}$ at the lower flight legs for aircraft, MYJ, QNSE, MYNN2.5, MYNN3, and BouLac, respectively

The dropsonde data are used to additionally compare the BouLac model simulation with the measurements, where the model vertical profiles are taken at the release location of each dropsonde. The dropsondes are released between 1347 UTC and 1420 UTC; therefore, assuming stationarity, the 1400 UTC vertical model profiles are extracted for the comparison. The comparison of the BouLac simulation with the raw dropsonde data shows satisfactory agreement for both u and v components around the height of the flight legs (Fig. 3a,b) for most dropsondes, whereas potential temperature, θ, shows significant discrepancy, both in the magnitude and vertical structure (Fig. 3c). This is mostly due to the underestimation of low-level potential temperature in the northern portion of the flight legs. Also, the dropsonde θ profiles indicate a well-mixed boundary layer at the northern part of the flight legs, which the WRF model only reproduces partially. However, due to the strong Bora flow, Ri should be primarily influenced by the vertical wind shear (e.g. Mahrt and Gamage 1987), and so would somewhat alleviate the relatively large discrepancies between the modelled and measured θ, as far as the turbulence generation is concerned. To elucidate this, Ri calculated from the model and the dropsondes is depicted in Fig. 14. The dropsonde data are suitably smoothed to match the model vertical resolution. While comparing Ri will in general lead to larger errors due to the nature of its calculation, it is obvious that in cases with large discrepancies in θ (e.g. S1), the magnitudes of Ri compare better than those of θ.

Based on fair agreement of the BouLac simulation with the measurements, and the fact that it is a 1D local turbulence closure scheme without horizontal advection, we conclude that the turbulence pattern along the flight legs is predominantly due to vertical wind shear and/or buoyancy. Further inspection of individual terms in the TKE Eq. 7 from the BouLac simulation shows that only the vertical shear term contributes to the production of TKE (not shown). This suggests that horizontal advection or buoyancy effects have no significant role in the modelled along-coast turbulence structure. However, as correctly pointed out by a reviewer, the PBL parametrization schemes are frequently "fine-tuned" to reproduce realistic profiles, which means that the represented processes may "simulate" the effects of the neglected ones.

Journal: 10546-BOUN Article No.: 9697 MS Code: BOUN913.2 TYPESET DISK LE CP Disp.:2012/1/14 Pages: 19 Layout: Small

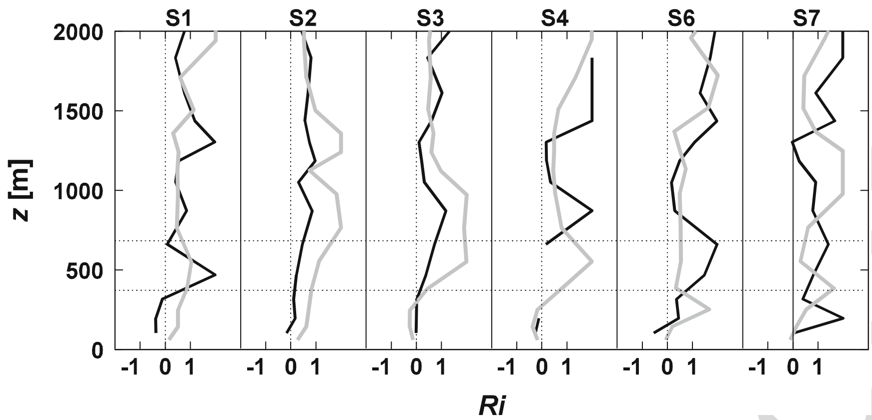

Fig. 14 Vertical profiles of the gradient Richardson number derived from six dropsondes (*black curves*) and from the WRF-ARW BouLac (Table 1) simulation (*grey curves*) in the spatial order from left to right from north-west towards south-east. The dropsonde data are suitably smoothed in order to correspond to the model vertical resolution. *Horizontal dotted lines* mark the altitude of the two flight legs. The modelled profiles are given for 1400 UTC 7 November 1999

Therefore, we cannot safely conclude that horizontal advection is unimportant in this case. On the other hand, the local vertical shear is probably the dominant TKE production factor, and it is safe to conclude that buoyancy has minor effects. It should be noted that Bougeault and Lacarrere (1989) did include the horizontal advection of TKE in Eq. 7 for their successful simulation of a Bora case, but the implementation of this and all other schemes in the WRF-ARW version used here is given without the advection term (Skamarock et al. 2008). The planned implementation of the horizontal advection in the boundary-layer schemes could resolve this issue.

6 Conclusions

This study addresses the along-coast turbulence structure of the Bora flow for a strong case observed in the lee of the Dinaric Alps on 7 November 1999 during MAP IOP 15. The data used are from the NCAR Electra aircraft and from dropsondes. Several different methods were used for determining the turbulence averaging interval, and the results are not conclusive. The fact that the averaging interval cannot be determined is attributed partly to the Bora heterogeneity in the along-flight direction. Therefore, we adopted a pragmatic approach in this study and focused only on the spatial variability of the normalized TKE for different averaging intervals. Significant spatial variability of TKE and the dissipation rate ε along the flight legs is revealed in this Bora case, associated with the attendant mesoscale phenomena, such as large amplitude mountain waves, wave breaking, jets, wakes and shear zones. As expected, the variations of TKE closely follow those of ε, which gives information about the robustness and consistency of the ε estimation. This is supported by good agreement in ε estimated using two different techniques inertial dissipation and the third-order structure function.

Since the origins of turbulence could not have been determined from the measurements alone, we used the WRF-ARW numerical model. Five simulations with different turbulence parametrization schemes (Table 1) reproduced the winds along the flight legs well, while potential temperature was systematically underestimated in the northern half of the flight legs. None of the simulations significantly outperformed the others in terms of the overall agreement of TKE with the measurements. However, the simulation using the BouLac turbulence parametrization scheme reproduced the spatial TKE structure along certain portions of the flight legs the best and was hence chosen for the study of the source of turbulence. The simulation suggests that the turbulence along the flight legs is produced by local vertical shear, i.e., that the horizontal TKE advection or buoyancy have no significant role in the along-coast Bora turbulence structure. However, given the uncertainties of the model simulation associated with the current turbulence parametrization schemes, the final confirmation of this conclusion awaits further evidence.

Acknowledgements We thank Alberto Martilli for help with the BouLac code and Larry Mahrt and Zoran Pasarić for useful discussions. Mathias Rotach and an anonymous reviewer are gratefully acknowledged for their comments that led to significant improvements of the study. This work was supported by the Croatian Ministry of Science, Education and Sports projects BORA 119-1193086-1311 and AQCT 119-1193086-1323. The National Center for Atmospheric Research is sponsored by the National Science Foundation.

References

Albertson JD, Parlange MB, Kiely G, Eichinger WE (1997) The average dissipation rate of turbulent kinetic energy in the neutral and unstable atmospheric surface layer. J Geophys Res 102:13423–13432

Baklanov A, Grisogono B (editors) (2007) Atmospheric boundary layers: nature, theory and applications to environmental modelling and security. Springer, New York, 241 pp

Balsley BB, Svensson G, Tjernstrom M (2008) On the scale-dependence of the gradient Richardson number in the residual layer. Boundary-Layer Meteorol 127:57–72

Batchelor GK (1959) The theory of homogeneous turbulence. Cambridge University Press, London, UK, 197 pp

Belušić D, Klaić ZB (2006) Mesoscale dynamics, structure and predictability of a severe Adriatic Bora case. Meteorol Z 15: 157–168. doi:10.1127/0941-2948/2006/0116

Belušić D, Pasarić M, Orlić M (2004) Quasi-periodic Bora gusts related to the structure of the troposphere. Q J Roy Meteorol Soc 130:1103–1121

Belušić D, Pasarić M, Pasarić Z, Orlić M, Grisogono B (2006) A note on local and non-local properties of turbulence in the Bora flow. Meteorol Z 15:301–306

Belušić D, Žagar M, Grisogono B (2007) Numerical simulation of pulsations in the Bora wind. Q J Roy Meteorol Soc 133: 1371–1388. doi:10.1002/qj.129

Biltoft CA (2001) Some thoughts on local isotropy and the 4/3 lateral to longitudinal velocity spectrum ratio. Boundary-Layer Meteorol 100:393–404

Bougeault P, Lacarrere P (1989) Parameterization of orography-induced turbulence in a mesobeta-scale model. Mon Weather Rev 117:1872–1890

Bougeault P, Binder P, Buzzi A, Dirks R, Houze R, Kuettner J, Smith RB, Steinacker R, Volkert H (2001) The MAP spetial observing period. Bull Am Meteorol Soc 82:433–462

Champagne FH (1978) The finescale structure of the turbulent velocity field. J Fluid Mech 86:67–108

Enger L, Grisogono B (1998) The response of Bora-type flow to sea surface temperature. Q J Roy Meteorol Soc 124:1227–1244

Gohm A, Mayr GJ, Fix A, Giez A (2008) On the onset of Bora and the formation of rotors and jumps near a mountain gap. Q J Roy Meteorol Soc 134:21–46

Grisogono B (2010) Generalizing “z-less” mixing length for stable boundary layers. Q J Roy Meteorol Soc 136:213–221

Grisogono B, Belušić D (2009) A review of recent advances in understanding the meso- and micro-scale properties of the severe Bora wind. Tellus A 61:1–16

Grubišić V (2004) Bora-driven potential vorticity banners over the Adriatic. Q J Roy Meteorol Soc 130: 2571–2603. doi:10.1256/qj.03.71

Heimann D (2001) Model-based wind climatology of the eastern Adriatic coast. Meteorol Z 10: 5–16. doi:10.1127/0941-2948/2001/0010-0005

Horvath K, Ivatek-Šahdan S, Ivančan-Picek B, Grubišić V (2009) Evolution and structure of two severe cyclonic Bora events: Contrast between the northern and southern Adriatic. Weather Forecast 24: 946–964

Howell JF, Mahrt L (1997) Multiresolution flux decomposition. Boundary-Layer Meteorol 83:117–137

Janjić ZI (1994) The step-mountain eta coordinate model: Further developments of the convection, viscous sublayer, and turbulence closure schemes. Mon Weather Rev 122:927–945

Jeromel M, Malačič V, Rakovec J (2009) Weibull distribution of Bora and sirocco winds in the northern Adriatic Sea. Geofizika 26:85–100

Jiang QF, Doyle JD (2005) Wave breaking induced surface wakes and jets observed during a Bora event. Geophys Res Let 32:L17807. doi:10.1029/2005GL022398

Jurčec V (1981) On mesoscale characteristics of Bora conditions in Yugoslavia. Pure Appl Geophys 119: 640–657

Kaimal JC, Finnigan JJ (1994) Atmospheric boundary layer flows: their structure and measurements. Oxford University Press, Oxford, 275 pp

Klaić ZB, Belušić D, Grubišić V, Gabela L, Ćoso L (2003) Mesoscale airflow structure over the northern Croatian coast during MAP IOP 15—a major Bora event. Geofizika 20:23–61

Klemp JB, Durran DR (1987) Numerical modelling of Bora winds. Meteorol Atmos Phys 36:215–227

Lenschow DH, Miller ER, Friesen RB (1991) A three-aircraft comparison of two types of air motion measurement systems. J Atmos Oceanic Technol 8:41–50

Mahrt L, Gamage N (1987) Observations of turbulence in stratified flow. J Atmos Sci 44:1106–1121

Mauritsen T, Svensson G, Zilitinkevich S, Esau I, Enger L, Grisogono B (2007) A total turbulent energy closure model for neutral and stably stratified atmospheric boundary layers. J Atmos Sci 64:4113–4126

Mellor GL, Yamada T (1974) A hierarchy of turbulence closure models for planetary boundary layers. J Atmos Sci 31:1791–1806

Mestayer PG (1982) Local isotropy and anisotropy in a high-Reynolds-number turbulent boundary layer. J Fluid Mech 125:475–503

Metzger M, Holmes H (2008) Time scales in the unstable atmospheric surface layer. Boundary-Layer Meteorol 126:29–50

Nakanishi M, Niino H (2006) An improved Mellor–Yamada level-3 model: its numerical stability and application to a regional prediction of advection fog. Boundary-Layer Meteorol 119:397–407

Oncley SP, Friehe CA, Businger JA, Itsweire EC, LaRue JC, Chang SS (1996) Surface layer fluxes, profiles and turbulence measurements over uniform terrain under near-neutral conditions. J Atmos Sci 53:1029–1044

Piper M, Lundquist J K (2004) Surface layer turbulence measurements during a frontal passage. J Atmos Sci 61:1768–1780. doi:10.1175/1520-0469(2004)061<1768:SLTMDA>2.0.CO;2

Poje D (1992) Wind persistence in Croatia. Int J Clim 12:569–586

Poje D (1995) Bura (Bora) and burin at Split. Croat Meteorol J 30:1–19

Skamarock WC, Klemp JB, Dudhia J, Gill DO, Barker DM, Duda MG, Huang X-Y, Wang W, Powers JG (2008) A description of the Advanced Research WRF version 3. NCAR/TN-475+STR

Smith RB (1987) Aerial observations of Yugoslavian Bora. J Atmos Sci 44:269–297

Stull RB (1988) An introduction to boundary layer meteorology. Kluwer, Dordrecht, 666 pp

Sukoriansky S, Galperin B, Perov V (2005) Application of a new spectral theory of stably stratified turbulence to the atmospheric boundary layer over sea ice. Boundary-Layer Meteorol 117:231–257

Telišman Prtenjak M, Belušić D (2009) Formation of reversed lee flow over the north-eastern Adriatic during Bora. Geofizika 26:145–155

Tennekes H, Lumely J (1972) A first course in turbulence. MIT Press, Cambridge, 300 pp

Trošić T, Trošić Ž (2010) Numerical simulation and observational analysis of the Bora of Pag's Ribs. Boundary-Layer Meteorol 134:353–366

Večenaj Ž, Belušić D, Grisogono B (2010) Charasteristics of the near-surface turbulence during a Bora event. Ann Geophy 28:155–163

Večenaj Ž, De Wekker SFJ, Grubišić V (2011) Near surface characteristics of the turbulence structure during a mountain wave event. J Appl Meteorol Clim 50:1088–1106

Vickers D, Mahrt L (2003) The cospectral gap and turbulent flux calculations. J Atmos Oceanic Technol 20:660–672

Vickers D, Mahrt L (2006) A solution for flux contamination by mesoscale motions with very weak turbulence. Boundary-Layer Meteorol 118:431–447

Wyngaard JC (2004) Toward numerical modeling in the "Terra Incognita". J Atmos Sci 61:1816–1826

Wyngaard JC (2010) Turbulence in the atmosphere. Cambridge University Press, New York, 393 pp

Zilitinkevich S, Elperin T, Kleeorin N, Rogachevskii I, Esau I, Mauritsen T, Miles MW (2008) Turbulence energetics in stably stratified geophysical flows: strong and weak mixing regimes. Q J Roy Meteorol Soc 134:793–799

Journal: 10546-BOUN Article No.: 9697 MS Code: BOUN913.2 TYPESET DISK LE CP Disp.:2012/1/14 Pages: 19 Layout: Small